Journal of Materials Chemistry C

ROYAL SOCIETY OF CHEMISTRY

PAPER

View Article Online
View Journal | View Issue

Cite this: J. Mater. Chem. C, 2020, 8, 15189

Correlating structural changes with the photophysics of terrylenediimide films during spontaneous annealing†

Natalia E. Powers-Riggs, Itai Schlesinger and Michael R. Wasielewski *

Received 13th June 2020,
Accepted 27th July 2020

DOI: 10.1039/d0tc02814b

rsc.li/materials-c

Interchromophore distance and geometry determine the nature of intermolecular coupling and therefore the photophysical behavior of the system. Here we demonstrate the close relationship between molecular orientation and coupling by characterizing the initial and final states of a *N*,*N*-bis(tricosan-12-yl)terrylene-3,4:11,12-bis(dicarboximide) (**C_{23}TDI**) film undergoing spontaneous annealing at room temperature. Appending long aliphatic tails to the large TDI π-surface produces an initially liquid crystal-like structure that reorganizes to the thermodynamically stable structure at room temperature. Monitoring the structural changes using UV-vis absorption and X-ray diffraction techniques reveals metastable intermediates we can identify and characterize, and the slow timescale of this change allows for a clear comparison between interchromophore structures and photophysical behavior at various points along the reaction coordinate, providing important insights into the relationship between chromophore packing and function. Initially upon film preparation, **C_{23}TDI** exhibits no long-range order but shows strong charge-transfer (CT) interactions, as observed through steady-state and transient absorption measurements. Within 60 hours under ambient conditions, the TDI units in the film reorganize to an orientation with higher crystallinity and diminished CT interaction, highlighting the dominance of long alkyl chain interactions over π-stacking interactions.

Introduction

Rylene diimides (RDIs) are a class of organic dyes that demonstrate robust stability,[1] numerous pathways for synthetic tunability,[2] and strong absorption of visible light.[3] They have been studied at length in a variety of applications,[4] including organic photovoltaics,[5–7] field-effect transistors,[8,9] and fluorescent dyes.[10] They are also invaluable for providing a fundamental understanding of excited-state dynamics of organic chromophores. The large π-surface of RDIs allows for many interchromophore geometries, which can disrupt or enhance absorbance and emission properties of a chromophore aggregate,[11–14] as well as influence charge/exciton delocalization and electron mobility. The coupling results from the spatial overlap between chromophores, with contributions from both of long-range coulombic (J_{coul}) and short-range charge-transfer (J_{CT}) coupling terms. The dependence of RDI electronic coupling strengths on interchromophore geometries has been examined previously through simulations,[11,13,15] as well as through studies of covalent dimers with well-defined through-bond[16] or through-space[17–19] interactions, hydrogen-bonding induced assemblies,[20] as well as films with different π-stacking patterns.[12,21,22] Some of these structures, such as the covalent dimers, are fixed, but other systems rely on self-assembly mechanisms to direct the nature of aggregation.

Of the systems ordered through self-assembly, thin films are a particularly valuable tool for gaining fundamental understanding of structure and function in organic electronics.[21] As an analogue for an active layer material, thin films reveal the nature of chromophore stacking,[23] allowing us to explore the relationship between molecular design and crystal packing,[24,25] as well as observe annealing affects.[26–28] Thin films are also well-suited to optical experiments to characterize steady-state and time-resolved photophysical behavior.[29–31] These kinds of systems have been used to study fundamental processes in bulk heterojunction blends,[32,33] and can be used for single layer materials, from charge generation through symmetry breaking to minimize V_{oc} loss,[34] or maximizing emission of fluorescent dyes.[35]

In RDI films, structural order can be engineered by adding steric modifiers at the imide position or to the aromatic core directly.[5,15,36] Common synthetic modifications include alkyl[37–41] or glycol tails,[39] or aryl rings,[26,42] which can direct microscale order as well as affect chromophore packing behaviors at a molecular level. Alkyl and aryl additions to the aromatic core

Department of Chemistry and Institute for Sustainability and Energy at Northwestern, Northwestern University, 2145 Sheridan Road, Evanston, Illinois 60208-3113, USA. E-mail: m-wasielewski@northwestern.edu

† Electronic supplementary information (ESI) available: Synthesis, additional optical spectra, X-ray scattering data, additional transient absorption data. See DOI: 10.1039/d0tc02814b

can cause increased slip-stacking between RDI moieties, while branched alkyl tails can lead disruption between π–π overlap by inducing rotation.[36,39]

To maximize order, films are frequently subjected to annealing conditions to reach a thermodynamic minimum, either by heating the film or by exposing it to solvent vapor.[36,43] Although these methods are often effective at producing crystalline order in films, it can be challenging to observe the onset of crystallization while simultaneously applying the annealing conditions[43,44] in order to better establish design principles for optimum film formation. An ideal system for elucidating the structure–function relationship would be one that can form two distinct packing arrangements and undergo reorganization without requiring external stimuli on a timescale that enables direct probing. Structural changes of liquid-crystalline thin films have been reported, but limited characterization of the photophysics has been discussed.

In comparison to perylene-3,4:9,10bis(dicarboximide) (PDI), terrylene-3,4:11,12-bis(dicarboximide) (TDI) has been studied to a lesser extent. Like other RDIs, TDI is a highly stable chromophore with a large extinction coefficient ($\sim$93 000 cm M^{-1} at 650 nm),[45] and has been used as a nonfullerene acceptor,[46,47] dye,[48,49] and fluorophore,[10,45,50] but its extended aromatic core introduces a higher propensity toward π-stacking and increased number of possible interchromophore geometries. In specific geometries with optimal electronic coupling,[36,51,52] TDI has been shown to undergo singlet fission with a neighboring chromophore to produce two triplet excitons.[53] In other coupling geometries, the excitation can delocalize across neighboring TDI units to produce an excimer,[36] and in closely packed configurations an excited TDI moiety will fully undergo symmetry-breaking charge transfer with a neighboring chromophore.[54]

Pairing the large aromatic surface of TDI with long aliphatic tails, as in the case of, *N*,*N*-bis(tricosan-12-yl)TDI (**C_{23}TDI**), reveals the role of each in the crystallinity. While TDI aggregates have been previously reported,[37] increased crystallinity within the thin-film was achieved through temperature changes or solvent vapor annealing.[36] Previous examinations of **C_{23}TDI** addressed aggregation behavior in different solvents and reported absorption for an annealed thin film.[55] Here, we monitor the structural evolution of a **C_{23}TDI** film during spontaneous thermal annealing in real time and correlate the changes in structure to its photophysics as the film ages. Upon preparation of **C_{23}TDI** films on a glass substrate, the long tails induce a spontaneous reorganization at room temperature. This reorganization occurs independent of external stimuli and can be observed through both changes in optical absorption and X-ray diffraction, which provides real-time insight into the relationship between structure and function of this system. Using this system, we gain a deeper understanding of the nature of film reorganization, as well as structural and photophysical information from two distinct states of the same molecule.

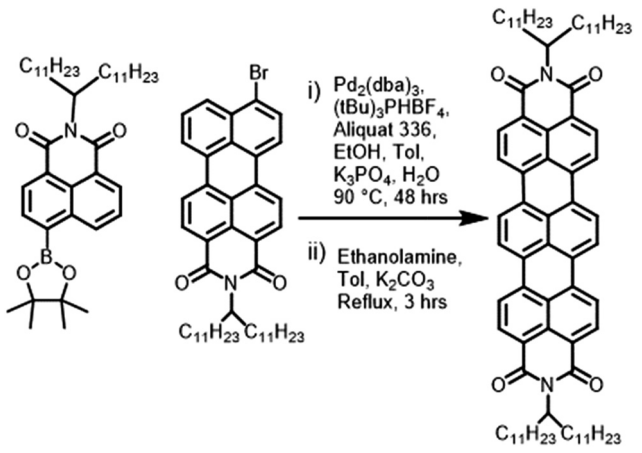

Scheme 1 Synthetic scheme for **C_{23}TDI**.

Experimental

Synthesis and film preparation

C_{23}TDI was synthesized following established preparations (Scheme 1).[2] Briefly, Suzuki coupling of perylene- and naphthalene monoimide precursors followed by cyclization produced **C_{23}TDI** in good yield (see ESI†).

Films were prepared by spin coating a glass slide with a concentrated ($\sim$1 mg mL^{-1}) solution of **C_{23}TDI** in THF. Solutions of chloroform or dichloromethane produced films with the same structural and photophysical properties as those prepared with THF. Films from higher concentration ($\sim$2 mg mL^{-1}) solutions were also prepared and similarly characterized, and differences in behavior are discussed below.

Steady-state spectroscopy

Spectra were obtained at room temperature on a Shimadzu 1800 UV-vis spectrometer. Emission spectra were collected on a Horiba Nanolog fluorimeter using a front-face arrangement of the excitation source and detector. All emission spectra were corrected for monochromator wavelength dependence and CCD-detector spectral response functions. Integration times 2 s were used to record spectra of both fresh and aged films.

Transient absorption spectroscopy

Femtosecond transient absorption spectroscopy (fsTA) experiments were performed using a regeneratively-amplified Ti:sapphire laser system (Tsunami oscillator/Spitfire Pro amplifier, Spectra-Physics) as previously described.[56] The excitation pulses were generated with a lab-built optical parametric amplifier.[57] The samples were irradiated at λ_{ex} = 585 nm with $\sim$110 fs, 0.6 μJ pulses and depolarized (DPU-25-A, Thorlabs, Inc) to suppress polarization-dependent signals. Transient spectra were acquired with 4 s averaging at each time delay point. The instrument response was about 300 fs.

X-ray diffraction and scattering

Grazing incidence X-ray scattering measurements were obtained at Beamline 8-ID-E of the Advanced Photon Source at Argonne National Laboratory. The X-ray beam (10.92 keV, 1.6868 Å) penetrated the sample at an incident angle of 0.14° to

maximize film scatter and minimize background scatter from the glass substrate. A Pilatus 1 M detector positioned 228 mm from the sample was used to collect the scattered light. Scattering intensity is reported as a function of the modulus of the scattering vector q, related to the scattering distance d spacing by $q = 2\pi/d$, and to the angle 2θ by the equation $q = (4\pi/\lambda)\sin(2\theta/2)$, where λ is the X-ray wavelength. GIXSGUI,[58] a MATLAB-based program, was used to apply pixel efficiency, polarization, flat field, and solid angle corrections to the detector images, as well as to display images and perform line cuts.

Powder X-ray diffraction (PXRD) data were collected at room temperature on a STOE-STADI-P powder diffractometer equipped with an asymmetric curved germanium monochromator (CuKα1 radiation, λ = 1.54056 Å) and one-dimensional silicon strip detector (MYTHEN2 1 K from DECTRIS). The line focused Cu X-ray tube was operated at 40 kV and 40 mA. Powder was packed in a 3 mm metallic mask and sandwiched between two layers of polyimide tape. Intensity data from 2θ = 1 to 35 degrees were collected over a period of 8 min in transmission mode with fixed $2\theta/\omega$ coupling of 2 : 1. The instrument was calibrated against a NIST Silicon standard (640d) prior the measurement. GSAS-II[59] was used for peak indexing and rigid body modeling.

Atomic force microscopy

Atomic Force Microscopy (AFM) images were taken using a home-built AFM system. The AFM was operated in contact mode using a soft (k = 0.2 N m^{-1}) cantilever (ContE-G, Budget Sensors) with minimal (~10 nm) deflection. All scans were taken in air and at room temperature. Before each AFM scan a UV-Vis spectrum of a **C_{23}TDI** sample prepared together with the AFM sample was taken.

Results and discussion

Ground-state dynamics

In comparison to a solution sample of **C_{23}TDI**, a freshly prepared film displays broadening and red-shifting in the steady-state absorption spectrum (Fig. 1). The 0–0 and 0–1 vibronic peaks appear at 680 and 620 nm in the film, rather than the 650 and 595 nm peaks observed in solution. The inverted peak ratio indicates H-aggregation according to zero-order models of coulombic coupling, suggesting close cofacial packing between TDI aromatic cores.[60] The film spectrum lacks the characteristic hypsochromic shift associated with H-aggregates suggested by Kasha,[61] indicating other coupling contributions are at play, including those from Frenkel excitons or charge-transfer (CT) states, due to direct overlap of molecular wavefunctions and quadrupolar interactions from the large aromatic cores of TDIs.[15,18,62]

Within 60 hours of film preparation, the absorption spectrum undergoes a dramatic shift at room temperature, displaying a major peak at 540 nm, with the intensity of the 705 nm 0–0 transition greatly reduced (Fig. 1, purple curve). This blue-shifted peak is better described by the standard Kasha exciton

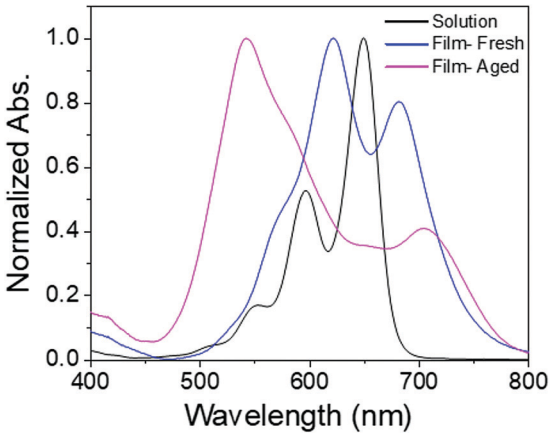

Fig. 1 Steady-state absorption spectra of **C_{23}TDI** in THF solution, (black), freshly prepared film (blue), and aged film (purple).

model of an H-aggregated state, suggesting a side-by-side alignment of dipole moments, but weaker short-range CT coupling between TDI moieties.[63] Emission data support the concept of differences in photophysical behavior resulting from changes in CT coupling. While both fresh and aged films display broad, red-shifted emission features, the emission for the fresh film is much less intense, indicating a largely non-emissive population, common for CT states (Fig. S1, ESI†). As the CT coupling contribution lessens, the intensity increases.

The phase transformation is observed under the presence or absence of light and oxygen and occurs on films prepared from concentrated solutions of both dichloromethane and tetrahydrofuran. In addition, we have observed a strong temperature dependence; at 60 °C, the transformation is complete within 30 min (Fig. S2, ESI†), while at lower temperatures the process is considerably slower. Films stored at 8 °C transformed completely in seven days, while films maintained in −22 °C retained their initial absorption spectrum after 21 days (Fig. S3, ESI†). Once the films reach the final state, further time and heating do not change the absorption spectrum, indicating this state is most likely the thermodynamic minimum. Dissolving the films yields a **C_{23}TDI** solution with the same absorption spectrum as the initial solutions, affirming that the absorption change is purely due to molecular reorganization in the solid state.

Steady-state absorption spectra at room temperature were collected every 30 minutes and show the progressive reorganization of the film (Fig. 2a). Two clear isosbestic points at 720 nm and 592 nm indicate the transformation of one distinct state into another. Plotting the absorption (A) at representative wavelengths of 542, 623, and 680 nm with respect to time yields the transformation kinetics. The kinetics at $t < 5$ h are complex; however, when $t > 5$ h the three wavelengths can be fit with the two-part sigmoidal equation:

$$A = A_0 + \alpha\left[\frac{p}{1+e^{\left(\frac{t-t_1}{\tau_1}\right)}} + \frac{1-p}{1+e^{\left(\frac{t-t_2}{\tau_2}\right)}}\right] \quad (1)$$

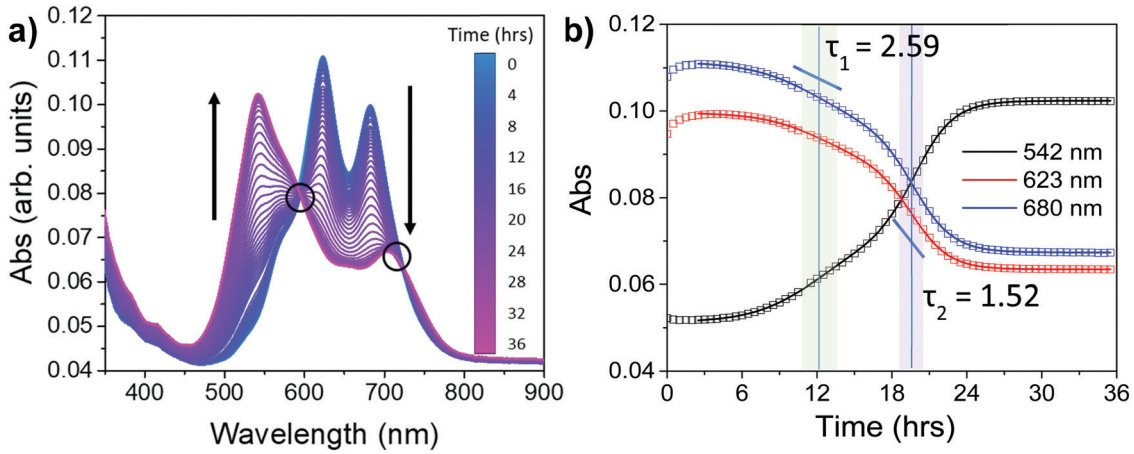

Fig. 2 (a) Steady-state absorption spectra of **C_{23}TDI** film, collected in 30 minutes increments. Isosbestic points are circled. (b) Kinetic traces of representative wavelengths (open squares), with fits to eqn (1) (solid lines).

where A_0 and α refer to the initial intensity offset and range, respectively. This equation describes two decay components with fractions p and $1 - p$ that have time offsets t_1 and t_2 and lifetimes of τ_1 and τ_2, respectively. For a film with an initial absorption of 0.11 at λ_{max} = 621 nm, globally fitting three wavelengths provides a self-consistent parameter set, and yields two components that constitute 36% and 64% of the total population, with time offsets 12.2 ± 0.2 and 19.8 ± 0.1 h, and lifetimes of 2.6 ± 0.1 and 1.5 ± 0.1 h, respectively. An additional film was prepared from a higher concentration solution, resulting in an initial absorption of 0.15 at λ_{max} = 621 nm. Here, the transformation occurs more slowly, but can be fit to the same equation, indicating some dependence on film thickness (Fig. S4, ESI†).

These consistent changes indicate that an initial reorganization upon film preparation produces a metastable state. At very early times (t < 5 h), peaks at 623 and 680 nm increase in intensity, indicating the existence of a local minimum. Following an induction period, this state first begins a slow transition, followed by a more rapid transition to achieve complete reorganization into the final, thermodynamically stable state. While the extended π-surface of the TDI likely directs the initial conformation, the long aliphatic tails promote the final ordered state.

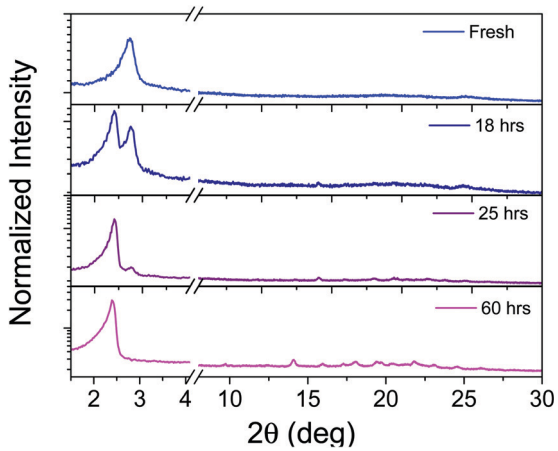

Fig. 3 PXRD spectra of bulk **C_{23}TDI** powder, with time after solvent evaporation.

Structural characterization

The slow structural transformation timescale in the **C_{23}TDI** film at room temperature creates an opportunity to observe structural reorganization to support the changes in absorption. The long alkyl tails on **C_{23}TDI** prevent the growth of a single crystal suitable for diffraction, the common starting point for thin-film structural analysis,[64,65] but X-ray scattering analysis of both film and powder samples of **C_{23}TDI** provide valuable insights into the possible packing geometries of the compound.

A concentrated solution of **C_{23}TDI** was dried to a film and immediately scraped off upon solvent evaporation; this powder was examined through PXRD at 0, 18, 25, and 60 hours after evaporation (Fig. 3). At early times, the sample is largely amorphous, but displays a peak at 2θ = 2.7°, corresponding to a spacing of 32 Å, and a broad peak around 25°, or 3.5 Å, indicating a high degree of π-stacking between **C_{23}TDI** moieties. After 60 hours, the powder develops higher crystallinity, and the lowest 2θ value shifts to 2.39°, corresponding to an extension of the longest axis of the unit cell to 37 Å, likely the result of straightening alkyl tails. This shift indicates a structural change between two conformations and correlates with the timescale observed by absorption.

Grazing incidence X-ray Scattering (GIWAXS) scans were collected on two glass substrate films at two time points each, one at 5 and 15 h, and another at 18 and 21 h after preparation, as well as for an aged film (Fig. S6, ESI†). Additionally, a film prepared on a glass slide with *n*-butyl tails attached to the surface prior to spin-coating the chromophore was measured at 22 and 32 hours. The features of the film generated on the butylated surface agree well with those observed from bare SiO_2 substrates in both GIWAXS (Fig. S6, ESI†) and steady-state absorption measurements (Fig. S5, ESI†), which indicates the reorganization is not surface dependent. While each film has a unique rate of reorganization depending on thickness and

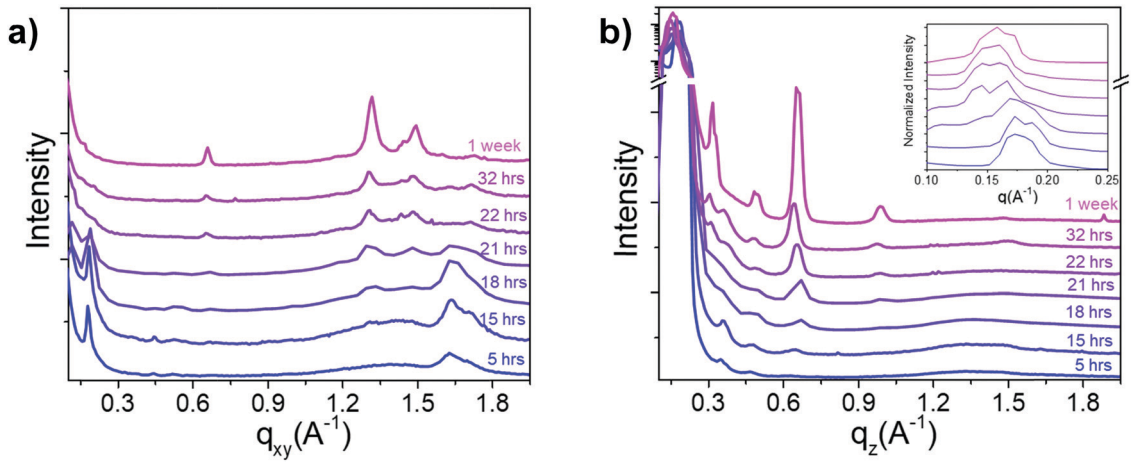

Fig. 4 GIWAXS scans of **C_{23}TDI** films: horizontal (a) and vertical (b) linecuts of films at various time points after film preparation. Inset shows magnified small q region.

homogeneity, these time points illustrate the general transformation trend with structural level detail. At early times, peaks in the q_{xy} direction at q = 1.7 Å^{-1} indicate packing with 3.8 Å spacing in the plane of the substrate (Fig. 4a), indicating an edge-on π-stacked orientation. As the film ages, these peaks disappear and are replaced by sharper peaks at smaller q values, pointing to the loss of direct π-stacking between chromophores. In the out-of-plane q_z direction, the growth of several features for the longer-aged films indicates the arrival at a final conformation with increased crystallinity. At low q values (q = 0.155 Å^{-1}, d = 40 Å), a high intensity peak suggests that the long axis of the unit cell lies normal to the surface of the film, or an edge-on orientation (Fig. 4b, inset). The shift of this peak to smaller q values over time indicates an initial state with a smaller unit cell axis, which grows over time, closely matching the observations from the PXRD data.

In addition to peaks along the q_{xy} and q_z axes, the aged **C_{23}TDI** film displays several sharp diffraction peaks, indicating a highly ordered structure. Integrating the GIWAXS pattern across all angles with respect to q yields a 1-dimensional diffraction pattern that, when converted from q to 2θ, agrees well with the PXRD scan after 60 hours, thus we surmise that the observed transformation occurs in both deposited films and bulk powder (Fig. 5a).

A unit cell was then extracted from the integrated GIWAXS data. The 2D image elucidates the Miller indices corresponding to specific peaks in the 1D spectrum; most notably, the broad peak at 2θ = 9.4° results from diffraction along an axis normal to the glass substrate, and the peak at 2θ = 13.5° does not lie along either the q_z or q_{xy} axes. GSAS-II software was used to identify a triclinic P1 unit cell (Table 1) which agrees well with the experimentally derived diffraction pattern as shown in Fig. 5b. The calculated unit cell volume of 2025.9 Å^3 indicates the number of **C_{23}TDI** molecules per unit cell is 1, following the formula suggested by Girolami.[66]

Using the parameters provided by this unit cell, we can infer some details about the nature of stacking in aged **C_{23}TDI** films.

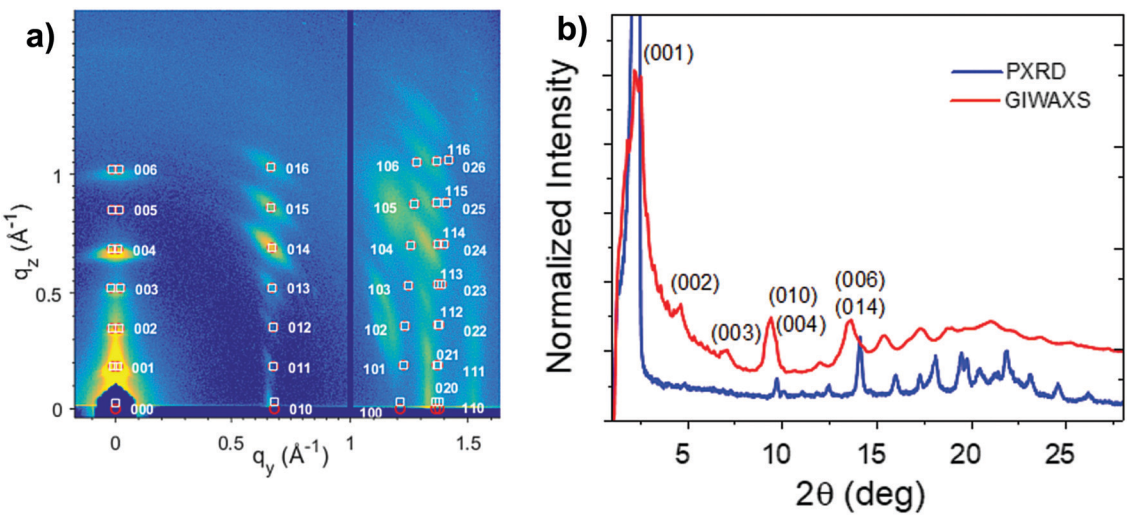

Fig. 5 (a) Overlay of diffraction peaks for extracted unit cell on 2D GIWAXS pattern and Miller indices. (b) Overlay of diffraction patterns of bulk powder (blue) and radially integrated line cut of GIWAXS data from film (red).

Table 1 Unit cell parameters

a (Å)	b (Å)	c (Å)	α (°)	β (°)	γ (°)	V (Å^3)
5.90	9.22	37.37	89.34	92.26	86.35	2026.9

Having one molecule per unit cell indicates all **C_{23}TDI** moieties are related by translation to other unit cells, and not by internal symmetry elements. This precludes TDI moieties experiencing rotational offsets in their stacking, as seen in *N*,*N*-bis(pentan-3-yl)TDI films,[36] which rely on glide plane symmetry elements. The blue-shifted absorption spectrum is indicative of long-range dipolar (coulombic) coupling between the aromatic cores of TDI, but due to the large (>3.5 Å) cell axes and near-right-angle vertices, TDI moieties must be slipped along an axis to be close enough to experience coupling, thus also ruling out cofacial stacking.

The abundance of diffraction peaks in both the 2D GIWAXS plot and the PXRD pattern allows for further modeling, which supports the premise of a slip stacked TDI core in the absence of a solved crystal structure. Rigid body simulated annealing using the known molecular structure of **C_{23}TDI** provides an approximation of the molecular orientation within the unit cell. We searched for patterns that displayed peaks at $2\theta = 9.4°$ and 13.5°, which correspond to (004) and (014) reflections, respectively, seen in Fig. 5a. While a conclusive orientation was not able to be determined, the solution with the best fit shows TDI moieties that lie diagonally across the unit cell (Fig. 6a). The proposed model indicates that the TDI aromatic cores do not overlap cofacially, which inhibits strong, short-range charge transfer coupling J_{CT}. Slippage between TDI chromophores can be seen in Fig. 6b, as well as depicted with higher clarity in Fig. S6 (ESI†). Other, higher-residual solutions also yielded structures where the TDI cores were similarly slipped, indicating that this is likely a generic feature of the minimized geometry. Further discussion of the proposed structure can be found in the ESI.†

In contrast to the aged film, the fresh film did not display sufficient diffraction to derive a unit cell. Nonetheless, the peaks corresponding to 32 Å and 4 Å in both PXRD and GIWAXS measurements, in addition to the steady-state absorption indicative of strong coupling, we can predict a roughly cofacial orientation, as displayed in Fig. S7 (ESI†).

Surface topography

Atomic Force Microscopy (AFM) also provides additional understanding of **C_{23}TDI** reorganization. A film was prepared under the same conditions as described above and broken in two segments. One piece was monitored by AFM at several time intervals, maintaining the same scan domain throughout the experiment (Fig. 7a). Examination of the film one hour after deposition shows clear boundaries between material with 20–30 nm thickness as shown in red, and bare glass substrate in blue (roughness ~1 nm). These larger domains indicate clusters of material upon spin coating of the film. As time passes and reorganization begins, the boundaries become less distinct, the domains decrease in thickness and cover increased portions of the film. Several smaller islands begin to form, indicating a more even distribution of material across the surface of the film.

The other segment of the same film was monitored by steady-state absorption spectroscopy at the same time intervals (Fig. 7b). Notably, the changes in topography occur much more rapidly than changes in absorption: the difference between 1 and 15 hours, for instance, is distinct in the AFM image but

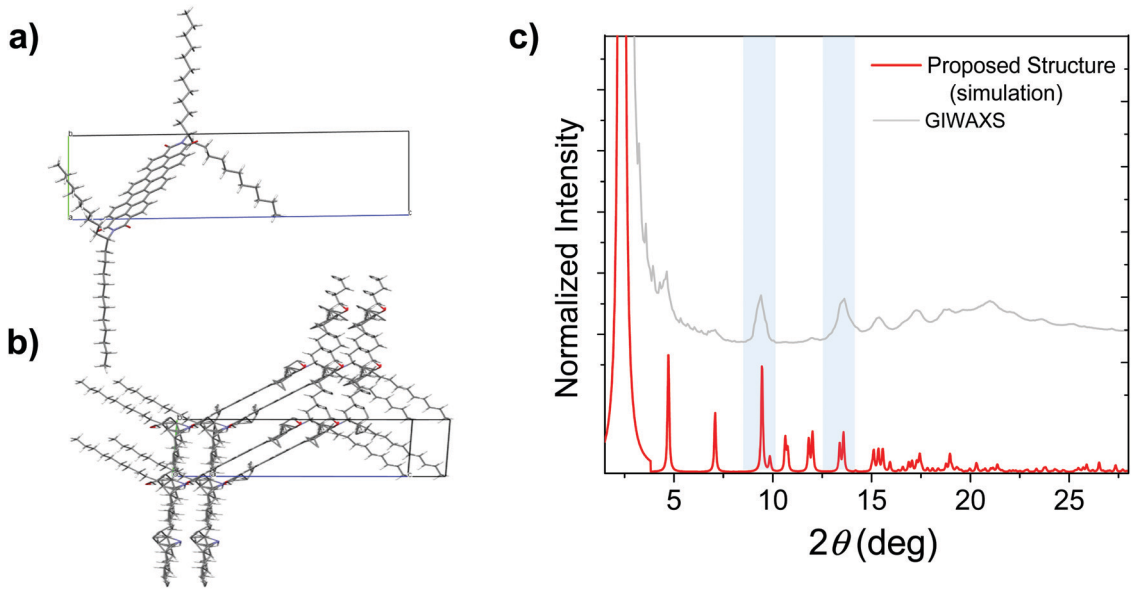

Fig. 6 (a) Proposed crystal structure unit cell from simulated annealing result. (b) Contents of 4 unit cells (2 × 1 × 2), rotated to highlight crystal packing. (c) Overlay of experimental GIWAXS spectrum of aged film (gray) and simulated powder patterns for simulated annealing result (red). Blue shading highlights regions of interest corresponding to (004) and (014) reflections.

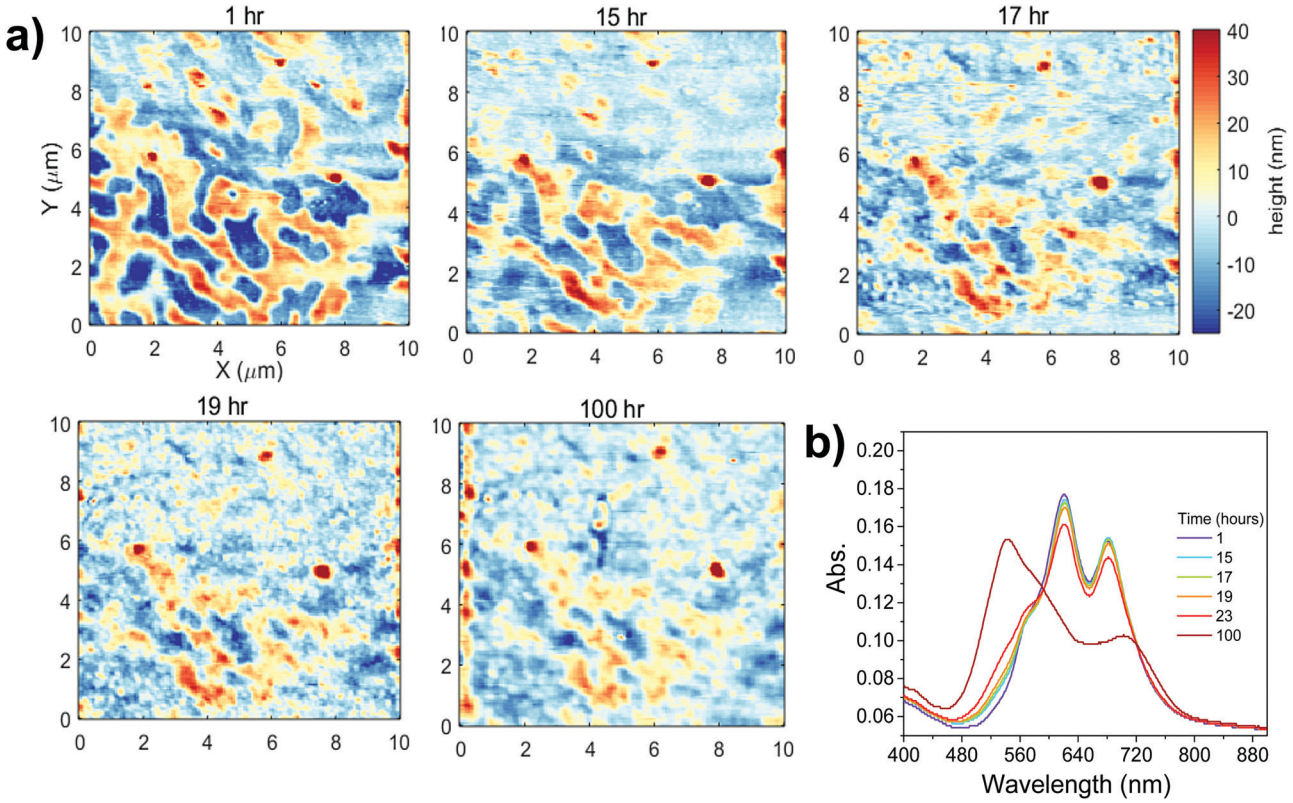

Fig. 7 (a) AFM topography at five time delays following film preparation. (b) Visible absorption spectra of film from the same preparation at identical time intervals.

barely noticeable in the absorption spectrum. The rapid changes in topography are likely due to alkyl tails "melting" – transitioning from their initial kinetic conformation to a thermodynamically stable conformation. This increased structural disorder creates an environment dominated by the liquid-crystalline behavior of the tails, allowing the aromatic surfaces of TDI to reorganize to a more stable conformation. This indicates two distinct processes in the film reorganization: first, a disruption of the initial metastable state into a disordered liquid crystalline state and second, reorganization of the chromophore cores. The first process changes the film topography but does not affect either the ordered chromophore spacing or transition dipole moments, so no changes are observed in X-ray scatter or absorption spectra. The second process involves clear changes in spacing and chromophore coupling, thus affecting the diffraction and absorption spectra, while showing little difference to the generally disordered surface of the film. Identifying the initial melting process explains the delayed onset of changes to the absorption spectrum.

Excited-state dynamics

In addition to affecting the ground state absorption, molecular packing plays an important role in the excited-state dynamics. Indeed, the excited-state behavior of **C_{23}TDI** varies dramatically between the fresh and aged film samples. For example, as noted above, the fluorescence emission from the fresh film is much less intense than that of the aged film.

The reason for this difference is apparent from an examination of their transient absorption spectra. Following excitation of the fresh sample at 590 nm, we observe the spectrum shown in Fig. 8. In the near infrared (NIR) region of the spectrum, we see broad absorptive features at 900, 1010, and 1330 nm; these features are consistent with reported spectra for TDI anion,[51,67] while the 1220 nm TDI singlet excited state absorption is notably absent. In the visible region, the 650 nm $TDI^{\bullet -}$ anion and 750 nm $TDI^{\bullet +}$ cation features are obscured by a broad ground-state bleach feature. Characteristic $TDI^{\bullet -}$ anion features imply symmetry-breaking charge separation similar to that previously observed in tightly stacked H-aggregates in solution.[54] This result is in good agreement with our proposition that the fresh sample has a cofacial stacking orientation and experiences strong charge-transfer interactions.

As is the case in the ground-state absorption spectrum, the excited state spectrum of the aged **C_{23}TDI** film indicates significantly less CT character than that of the fresh film. The NIR region displays a broad peak at 1100 nm, but no clear signatures of either singlet or $TDI^{\bullet -}$ anion absorptions. In the visible region, a broad ground-state bleach from 500 to 750 nm overlaps with a strong positive absorptive feature. These resultant spectra are more consistent with that of an excimer, similar to that observed in slip-stacked TDI films.[36] All features decay within 1 ns, which is consistent with the lack of triplet state present at long times. Further kinetic analysis is included in Fig. S7–S10 (ESI†).

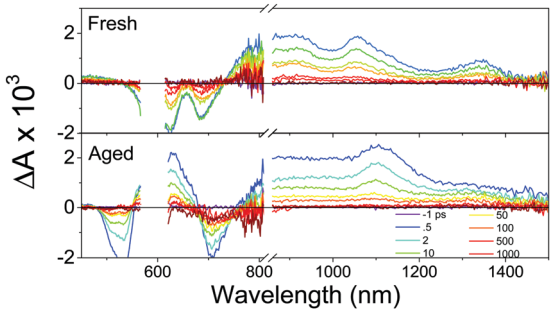

Fig. 8 Transient absorption spectra at selected decay times after excitation at λ_{ex} = 590 nm for both fresh and aged films.

The broadened signal and absence of a sharp 1330 nm TDI anion band indicate that the reorganized structure does not provide the optimal coupling that leads to SB-CS states in TDI. Instead, the excited state exhibits significantly more singlet character, resulting in the formation of an excimer, which is further supported by the increased emission compared to the fresh film. The greater singlet character of the excited state is in line with the conclusions for the ground-state spectrum as well. The ground-state spectrum of the aged film agrees better with that of an H-aggregate: the inverted peak ratio and dramatically blue-shifted spectrum are both characteristics of such a structure. Given the coupling map of perylene suggested by Hestand *et al.*,[60] the short- and long-axis slippage from the reorganized structure clearly has weaker J_{CT}.

These findings also have useful implications to the larger understanding of structural reorganization and its effect on light-absorbing processes for practical applications. Blended films, for instance, as would be found in a bulk heterojunction OPV device, typically exhibit varying degrees of phase segregation. In electron acceptor domains of **C_{23}TDI**, we expect rearrangement to proceed in the same manner as observed here. Indeed, given the ability of **C_{23}TDI** to reorganize at room temperature, it is likely phase segregation would occur in a blend. In the regions of true intercalation between **C_{23}TDI** and a donor material, reorganization is still likely to take place as the aliphatic tails melt, but additional additives may immobilize the aromatic core, making rearrangement unlikely.

Alternatively, in a single-layer OPV device where the dye acts as both the donor and acceptor, harnessing charges generated from symmetry-breaking charge transfer may prove fruitful by minimizing V_{oc} losses. For such applications, the conclusions from this paper highlight the value of strong coupling due to cofacial stacking. Conversely, in systems designed to promote emission, using aliphatic tails to disrupt cofacial interaction without requiring additional annealing steps could lead to more efficient device processing. In this way, the observations and conclusions of this study have broad implications for many different types of device applications. This work also provides a more fundamental understanding of the structural dynamics operating during annealing processes, as well as direct future researchers to systems that will not spontaneously rearrange.

Conclusions

Despite the large rigid core of TDI and its propensity to π-stack in more aggregating conditions, the long aliphatic tails allow the **C_{23}TDI** film to undergo spontaneous thermal annealing at room temperature. This transformation can be observed through changes in UV-vis absorption and crystallinity and tracking both reveals the close relationship between structure and function of the compound. The initial state in the freshly cast films is relatively disordered, but π-stacking peaks seen in X-ray measurements imply close packing between TDI aromatic cores, and both vibronic peak ratios in the ground-state and clear $TDI^{\bullet-}$ signals in the excited-state absorption indicate a large amount of J_{CT} between TDI moieties. Over time, the film increases in crystallinity, and the resultant structure comprises less overlap between TDI cores, observed through diffraction patterns and excimer features in the transient absorption spectra, indicating a greater contribution from the singlet state and reduced J_{CT}. These findings indicate that the dispersion interactions that drive the aggregation of saturated alkyl chains can overcome the strong π–π interactions intrinsic to the large aromatic core of TDI derivatives to elicit new packing motifs that may prove useful in modifying the opto-electronic properties of these chromophores.

Conflicts of interest

There are no conflicts to declare.

Acknowledgements

This work was supported by the U.S. Department of Energy, Office of Science, Office of Basic Energy Sciences under Award DE-FG02-99ER14999 (M. R. W.). N. E. P.-R. was supported by NSF Graduate Research Fellowship (DGE-1324585). I. S. would like to thank Yad Hanadiv Foundation for the Rothschild Postdoctoral Fellowship. Thanks to Ryan M. Young for discussion and support. Use was made of the IMSERC X-ray Facility at Northwestern University, which has received support from the Soft and Hybrid Nanotechnology Experimental (SHyNE) Resource (NSF ECCS-1542205); the State of Illinois and International Institute for Nanotechnology (IIN). Thanks to Dr Christos Malliakas for guidance in analyzing powder diffraction data. Thanks to Joaquin M. Alzola for collection of GIWAXS data and discussion. Use of the Advanced Photon Source, an Office of Science User Facility operated for the U.S. Department of Energy (DOE) Office of Science by Argonne National Laboratory, was supported by the U.S. DOE under Contract no. DE-AC02-06CH11357.

Notes and references

1 L. Chen, C. Li and K. Müllen, *J. Mater. Chem. C*, 2014, **2**, 1938–1956.
2 F. Nolde, J. Qu, C. Kohl, N. G. Pschirer, E. Reuther and K. Mullen, *Chemistry*, 2005, **11**, 3959–3967.

3 S. K. Lee, Y. Zu, A. Herrmann, Y. Geerts, K. Müllen and A. J. Bard, *J. Am. Chem. Soc.*, 1999, **121**, 3513–3520.
4 C. Huang, S. Barlow and S. R. Marder, *J. Org. Chem.*, 2011, **76**, 2386–2407.
5 P. E. Hartnett, A. Timalsina, H. S. S. R. Matte, N. Zhou, X. Guo, W. Zhao, A. Facchetti, R. P. H. Chang, M. C. Hersam, M. R. Wasielewski and T. J. Marks, *J. Am. Chem. Soc.*, 2014, **136**, 16345–16356.
6 J. Li, F. Dierschke, J. Wu, A. C. Grimsdale and K. Müllen, *J. Mater. Chem.*, 2006, **16**, 96–100.
7 X. Zhan, A. Facchetti, S. Barlow, T. J. Marks, M. A. Ratner, M. R. Wasielewski and S. R. Marder, *Adv. Mater.*, 2011, **23**, 268–284.
8 P. R. L. Malenfant, C. D. Dimitrakopoulos, J. D. Gelorme, L. L. Kosbar, T. O. Graham, A. Curioni and W. Andreoni, *Appl. Phys. Lett.*, 2002, **80**, 2517–2519.
9 A. Facchetti, *Mater. Today*, 2007, **10**, 28–37.
10 M. Davies, C. Jung, P. Wallis, T. Schnitzler, C. Li, K. Müllen and C. Bräuchle, *ChemPhysChem*, 2011, **12**, 1588–1595.
11 N. Renaud, P. A. Sherratt and M. A. Ratner, *J. Phys. Chem. Lett.*, 2013, **4**, 1065–1069.
12 A. K. Le, J. A. Bender, D. H. Arias, D. E. Cotton, J. C. Johnson and S. T. Roberts, *J. Am. Chem. Soc.*, 2018, **140**, 814–826.
13 J. Vura-Weis, M. A. Ratner and M. R. Wasielewski, *J. Am. Chem. Soc.*, 2010, **132**, 1738–1739.
14 S. Masoomi-Godarzi, C. R. Hall, B. Zhang, M. A. Gregory, J. M. White, W. W. H. Wong, K. P. Ghiggino, T. A. Smith and D. J. Jones, *J. Phys. Chem. C*, 2020, **124**, 11574–11585.
15 A. Oleson, T. Zhu, I. S. Dunn, D. Bialas, Y. Bai, W. Zhang, M. Dai, D. R. Reichman, R. Tempelaar, L. Huang and F. C. Spano, *J. Phys. Chem. C*, 2019, **123**, 20567–20578.
16 M. Chen, M. D. Krzyaniak, J. N. Nelson, Y. J. Bae, S. M. Harvey, R. D. Schaller, R. M. Young and M. R. Wasielewski, *Proc. Natl. Acad. Sci. U. S. A.*, 2019, **116**, 8178–8183.
17 J. Sung, A. Nowak-Krol, F. Schlosser, B. Fimmel, W. Kim, D. Kim and F. Wurthner, *J. Am. Chem. Soc.*, 2016, **138**, 9029–9032.
18 E. A. Margulies, L. E. Shoer, S. W. Eaton and M. R. Wasielewski, *Phys. Chem. Chem. Phys.*, 2014, **16**, 23735–23742.
19 Y. Hong, J. Kim, W. Kim, C. Kaufmann, H. Kim, F. Würthner and D. Kim, *J. Am. Chem. Soc.*, 2020, **142**, 7845–7857.
20 S. Ghosh, X.-Q. Li, V. Stepanenko and F. Würthner, *Chem. – Eur. J.*, 2008, **14**, 11343–11357.
21 D. E. Cotton, A. P. Moon and S. T. Roberts, *J. Phys. Chem. C*, 2020, **124**, 11401–11413.
22 S. W. Eaton, L. E. Shoer, S. D. Karlen, S. M. Dyar, E. A. Margulies, B. S. Veldkamp, C. Ramanan, D. A. Hartzler, S. Savikhin, T. J. Marks and M. R. Wasielewski, *J. Am. Chem. Soc.*, 2013, **135**, 14701–14712.
23 N. T. Shewmon, D. L. Watkins, J. F. Galindo, R. B. Zerdan, J. Chen, J. Keum, A. E. Roitberg, J. Xue and R. K. Castellano, *Adv. Funct. Mater.*, 2015, **25**, 5166–5177.
24 K. H. Lee, P. E. Schwenn, A. R. Smith, H. Cavaye, P. E. Shaw, M. James, K. B. Krueger, I. R. Gentle, P. Meredith and P. L. Burn, *Adv. Mater.*, 2011, **23**, 766–770.
25 R. Steyrleuthner, M. Schubert, I. Howard, B. Klaumünzer, K. Schilling, Z. Chen, P. Saalfrank, F. Laquai, A. Facchetti and D. Neher, *J. Am. Chem. Soc.*, 2012, **134**, 18303–18317.
26 B. A. Gregg, *J. Phys. Chem.*, 1996, **100**, 852–859.
27 O. K. Kwon, M. A. Uddin, J.-H. Park, S. K. Park, T. L. Nguyen, H. Y. Woo and S. Y. Park, *Adv. Mater.*, 2016, **28**, 910–916.
28 A. Sarbu, L. Biniek, J.-M. Guenet, P. J. Mésini and M. Brinkmann, *J. Mater. Chem. C*, 2015, **3**, 1235–1242.
29 G. Wang, S. M. Swick, M. Matta, S. Mukherjee, J. W. Strzalka, J. L. Logsdon, S. Fabiano, W. Huang, T. J. Aldrich, T. Yang, A. Timalsina, N. Powers-Riggs, J. M. Alzola, R. M. Young, D. M. DeLongchamp, M. R. Wasielewski, K. L. Kohlstedt, G. C. Schatz, F. S. Melkonyan, A. Facchetti and T. J. Marks, *J. Am. Chem. Soc.*, 2019, **141**, 13410–13420.
30 S. M. Falke, C. A. Rozzi, D. Brida, M. Maiuri, M. Amato, E. Sommer, A. De Sio, A. Rubio, G. Cerullo, E. Molinari and C. Lienau, *Science*, 2014, **344**, 1001–1005.
31 A. C. Jakowetz, M. L. Bohm, J. Zhang, A. Sadhanala, S. Huettner, A. A. Bakulin, A. Rao and R. H. Friend, *J. Am. Chem. Soc.*, 2016, **138**, 11672–11679.
32 N. D. Eastham, A. S. Dudnik, T. J. Aldrich, E. F. Manley, T. J. Fauvell, P. E. Hartnett, M. R. Wasielewski, L. X. Chen, F. S. Melkonyan, A. Facchetti, R. P. H. Chang and T. J. Marks, *Chem. Mater.*, 2017, **29**, 4432–4444.
33 N. D. Eastham, J. L. Logsdon, E. F. Manley, T. J. Aldrich, M. J. Leonardi, G. Wang, N. E. Powers-Riggs, R. M. Young, L. X. Chen, M. R. Wasielewski, F. S. Melkonyan, R. P. H. Chang and T. J. Marks, *Adv. Mater.*, 2018, **30**, 1704263.
34 A. N. Bartynski, M. Gruber, S. Das, S. Rangan, S. Mollinger, C. Trinh, S. E. Bradforth, K. Vandewal, A. Salleo, R. A. Bartynski, W. Bruetting and M. E. Thompson, *J. Am. Chem. Soc.*, 2015, **137**, 5397–5405.
35 E. Kozma, W. Mróz, F. Villafiorita-Monteleone, F. Galeotti, A. Andicsová-Eckstein, M. Catellani and C. Botta, *RSC Adv.*, 2016, **6**, 61175–61179.
36 E. A. Margulies, J. L. Logsdon, C. E. Miller, L. Ma, E. Simonoff, R. M. Young, G. C. Schatz and M. R. Wasielewski, *J. Am. Chem. Soc.*, 2017, **139**, 663–671.
37 F. Nolde, W. Pisula, S. Müller, C. Kohl and K. Müllen, *Chem. Mater.*, 2006, **18**, 3715–3725.
38 C. M. Mauck, P. E. Hartnett, E. A. Margulies, L. Ma, C. E. Miller, G. C. Schatz, T. J. Marks and M. R. Wasielewski, *J. Am. Chem. Soc.*, 2016, **138**, 11749–11761.
39 S.-G. Liu, G. Sui, R. A. Cormier, R. M. Leblanc and B. A. Gregg, *J. Phys. Chem. B*, 2002, **106**, 1307–1315.
40 P. E. Hartnett, E. A. Margulies, H. S. S. R. Matte, M. C. Hersam, T. J. Marks and M. R. Wasielewski, *Chem. Mater.*, 2016, **28**, 3928–3936.
41 K. Balakrishnan, A. Datar, T. Naddo, J. Huang, R. Oitker, M. Yen, J. Zhao and L. Zang, *J. Am. Chem. Soc.*, 2006, **128**, 7390–7398.
42 P. E. Hartnett, E. A. Margulies, C. M. Mauck, S. A. Miller, Y. Wu, Y. L. Wu, T. J. Marks and M. R. Wasielewski, *J. Phys. Chem. B*, 2016, **120**, 1357–1366.
43 V. Belova, B. Wagner, B. Reisz, C. Zeiser, G. Duva, J. Rozbořil, J. Novák, A. Gerlach, A. Hinderhofer and F. Schreiber, *J. Phys. Chem. C*, 2018, **122**, 8589–8601.
44 X. Jiao, C. Wang and C. R. McNeill, *Macromolecules*, 2019, **52**, 4646–4654.

45 S. Mais, J. Tittel, T. Basché, C. Bräuchle, W. Göhde, H. Fuchs, G. Müller and K. Müllen, *J. Phys. Chem. A*, 1997, **101**, 8435–8440.
46 J. Feng, N. Liang, W. Jiang, D. Meng, R. Xin, B. Xu, J. Zhang, Z. Wei, J. Hou and Z. Wang, *Org. Chem. Front.*, 2017, **4**, 811–816.
47 S. Stappert, C. Li, K. Müllen and T. Basché, *Chem. Mater.*, 2016, **28**, 906–914.
48 F. O. Holtrup, R. J. M. G. H. Quante, S. De Feyter, F. C. De Schryver and K. Mullen, *Chemistry*, 1997, **3**, 219–225.
49 Z. Yuan, S. L. Lee, L. Chen, C. Li, K. S. Mali, S. De Feyter and K. Mullen, *Chemistry*, 2013, **19**, 11842–11846.
50 C. Seebacher, C. Hellriegel, F.-W. Deeg, C. Bräuchle, S. Altmaier, P. Behrens and K. Müllen, *J. Phys. Chem. B*, 2002, **106**, 5591–5595.
51 E. A. Margulies, C. E. Miller, Y. Wu, L. Ma, G. C. Schatz, R. M. Young and M. R. Wasielewski, *Nat. Chem.*, 2016, **8**, 1120.
52 M. Chen, Y. J. Bae, C. M. Mauck, A. Mandal, R. M. Young and M. R. Wasielewski, *J. Am. Chem. Soc.*, 2018, **140**, 9184–9192.
53 M. B. Smith and J. Michl, *Chem. Rev.*, 2010, **110**, 6891–6936.
54 N. E. Powers-Riggs, X. Zuo, R. M. Young and M. R. Wasielewski, *J. Am. Chem. Soc.*, 2019, **141**, 17512–17516.
55 Z. Guo, X. Zhang, L. Zhang, Y. Wang, W. Feng, K. Sun, Y. Yi and Z. Li, *Front. Chem.*, 2019, **7**, 473.
56 R. M. Young, S. M. Dyar, J. C. Barnes, M. Juríček, J. F. Stoddart, D. T. Co and M. R. Wasielewski, *J. Phys. Chem. A*, 2013, **117**, 12438–12448.
57 S. R. Greenfield and M. R. Wasielewski, *Opt. Lett.*, 1995, **20**, 1394–1396.
58 Z. Jiang, *J. Appl. Crystallogr.*, 2015, **48**, 917–926.
59 B. H. Toby and R. B. Von Dreele, *J. Appl. Crystallogr.*, 2013, **46**, 544–549.
60 N. J. Hestand and F. C. Spano, *J. Chem. Phys.*, 2015, **143**, 244707.
61 M. Kasha, H. R. Rawls and M. Ashraf El-Bayoumi, *Pure Appl. Chem.*, 1965, **11**, 371–392.
62 N. J. Hestand and F. C. Spano, *Acc. Chem. Res.*, 2017, **50**, 341–350.
63 N. J. Hestand and F. C. Spano, *Chem. Rev.*, 2018, **118**, 7069–7163.
64 Y. J. Bae, X. Zhao, M. D. Kryzaniak, H. Nagashima, J. Strzalka, Q. Zhang and M. R. Wasielewski, *J. Phys. Chem. C*, 2020, **124**, 9822–9833.
65 T. N. Krauss, E. Barrena, X. N. Zhang, D. G. de Oteyza, J. Major, V. Dehm, F. Wurthner, L. P. Cavalcanti and H. Dosch, *Langmuir*, 2008, **24**, 12742–12744.
66 G. S. Girolami, *J. Chem. Educ.*, 1994, **71**, 962.
67 C. M. Mauck, Y. J. Bae, M. Chen, N. Powers-Riggs, Y. L. Wu and M. R. Wasielewski, *ChemPhotoChem*, 2018, **2**, 223–233.

